WhatEELS. A python-based interactive software solution for ELNES analysis combining clustering and NLLS.

Authors

Blanco-Portals, J.[1,2,*], Torruella, P.[1,2] ,Baiutti, F.[3], Anelli, S.[3] ,Torrel,M.[3],Tarancón, A.[3,4], Peiró, F.[1,2], Estradé, S.[1,2]

[1] LENS-MIND, Department of Electronics and Biomedical Engineering, Universitat de Barcelona, 08028 Barcelona, Spain

[2] Institute of Nanoscience and Nanotechnology (IN2UB), Universitat de Barcelona, 08028 Barcelona, Spain

[3] Catalonia Institute for Energy Research (IREC), Jardins de Les Dones de Negre 1, 08930 Sant Adrià del Besòs, Barcelona, Spain

[4] ICREA, 23 Passeig Lluís Companys, Barcelona 08010, Spain.

Corresponding author*: jblancoportals@gmail.com , jblanco@ub.edu

Abstract

The analysis of energy loss near edge structures in EELS is a powerful method for a precise characterization of elemental oxidation states and local atomic coordination with an outstanding lateral resolution, down to the atomic scale. Given the complexity and sizes of the EELS spectrum images datasets acquired by the state-of-the-art instrumentation, methods with low convergence times are usually preferred for spectral unmixing in quantitative analysis, such as multiple linear least squares fittings. Nevertheless, non-linear least squares fitting may be a superior choice for analysis in some cases, as it eliminates the need of calibrated reference spectra and provides information for each of the individual components included in the fitted model.

To avoid some of the problems that the non-linear least squares algorithms may suffer dealing with mixed-composition samples and, thus, a model comprised by a large number of individual curves we proposed the combination of clustering analysis for segmentation and non-linear least squares fitting for spectral analysis. Clustering analysis is capable of a fast classification of pixels in smaller subsets divided by their spectral characteristics, and thus increases the control over the model parameters in separated regions of the samples, classified by their specific compositions. Furthermore, along with this manuscript we provide access to a self-contained and expandable modular software solution called ***WhatEELS***. It was specifically designed to facilitate the combined use of clustering and NLLS, and includes a set of tools for white-lines analysis and elemental quantification. We successfully demonstrated its capabilities with a control sample of mesoporous cerium oxide doped with praseodymium and gadolinium, which posed challenging case-study given its spectral characteristics.

Keywords: Electron Energy Loss Spectroscopy (EELS), Energy Loss Near Edge Spectroscopy (ELNES), Non-linear Least Squares fitting (NLLS), Clustering Analysis, Oxidation State Analysis, Elemental Quantification.

1.Introduction

Transmission electron microscopy (TEM) and the core associated analytical tools (i.e., electron energy loss spectroscopy, EELS, and energy dispersive X-ray spectroscopy, X-EDS) have become a staple among all the characterization techniques in materials science, given their high spatial resolution and powerful analytical capabilities[1]. In particular, EELS stands out by its sensitivity to low atomic number elements and its superior lateral resolution[2–5]. Furthermore, the study of energy loss near edge structures (ELNES) in EELS spectra allows the identification of different oxidation states and atomic coordination numbers, reaching even the atomic scale resolution, in both a qualitative and a quantitative way[6–8].

When it comes to sample analysis via EELS spectroscopy, a direct quantification measurement based on the Egerton method will often suffice to characterize the material to the desired extent[9–12]. Some other well-known methodologies make use of the principal component analysis (PCA)[13] or independent component analysis (ICA)[14], dimensionality reduction algorithms used to isolate and identify specific regions with distinctive spectral features induced by local differences in composition or chemical state (e.g., high dopant concentration areas or changes in the oxidation states). PCA can even be used in combination with the aforementioned Egerton method[9], as a noise-reduction pre-step[15]. Nevertheless, PCA does not come without problems, namely user bias on the spectral base selection and interpretation and problems of non-compliant data samples[16–19]. Hence, further efforts are constantly being made to integrate new techniques into the standard EELS data-treatment arsenal.

In recent times, unsupervised clustering classifying algorithms (mainly K-means and hierarchical clustering) have been presented as fast methods to achieve a qualitative segmentation of the ever-increasing in size EELS datasets[20]. One major drawback to be noticed is the lack of a robust way to easily evaluate the accuracy of the clusters resolved, other than a later inspection by the user (i.e., always prone to some sort of bias). Also, if the sample presents areas with significant differences in thickness, the algorithms may lose effectivity (i.e., the total number of raw electron counts, dominated by thickness effects, will outweigh any minor spectral variation associated to the presence of trace elements or low dopant concentration areas). Nonetheless, it is a fast way to inspect large datasets and get an initial assessment of the presence of different areas in the sample segmented by spectral features.

Multiple linear least squares (MLLS) fitting creates a series of weighted maps for user-selected reference signals, that may be externally provided or extracted from the same dataset under analysis. It is a trusted method in the EELS community to get quantitative measurements[21–24], but its accuracy may suffer when facing dataset with marginal regions with small differences in compositions, given its dependency on the manually set references. The combined use of clustering and MLLS has been recently proposed as a way to overcome the bias when selecting these references, by using the centroids as the signals to be fitted[25].

Finally, the non-linear least squares (NLLS) method applied to EELS[26–28] consists of fitting a variety of individual curves (components) to get the best approximation of the given raw data. Usually, a combination of simple peak-like curves for the specific near edge features (e.g., Gaussians, Lorentzian and Pseudo-Voigt), and arctangent, power-law decays or cross-section curves (calculated by Hartree-Slater approximations or from hydrogenic models) for the continuum excitations, are carefully selected for each

edge on the spectra. The posterior analysis of the parameters of these curves is what makes NLLS a great choice to study particular ELNES characteristics[29], such as local variations in the atomic oxidation states, given that the most common reported methods of characterization in the literature are the white-line (WL) ratio variation measurements[30–32], the relative position of WLs and their distance to the onset of the oxygen edge[33] (computed by integrating the peak-like curves or measuring their centres after the fitting). Also, NLLS can be a valuable tool for elemental quantification in cases of heavily overlapping edges (e.g., samples of mixed cerium-praseodymium oxides[34]), as the fitting process is able to separate the electron counts belonging to different elements. One major drawback is that the NLLS data fitting process is usually slow, given the large number of parameters involved with each added component. Furthermore, the increment in convergence times is not linear with the number of components (i.e., adding a single extra curve to the fitting may dramatically increase the time it takes to finalize the fitting process, or even cause divergent results).

Several software tools are already available for EELS data analysis, that incorporate solutions for the aforementioned analysis and fitting techniques. The two more popular are Digital Micrograph (DM, currently on its third version, it is a proprietary tool from GATAN) and HyperSpy[35] (a free-software, python-based multidisciplinary spectroscopic tool). The main problem of DM is that most of the EELS and ELNES analysis tools, although powerful and reliable, are not distributed freely. HyperSpy is, arguably, the most popular free-software tool, continuously supported and updated by a sizable community of users. Nevertheless, when it comes to the specific task of EELS spectral fitting it may lack the speed for an efficient workflow. It also requires a minimum knowledge of Python language to be successfully used and for posterior analysis of the results, which often drives away potential users.

In this work, we present a new tool, specifically focused on ELNES analysis, ***WhatEELS*** (which is available at http://hdl.handle.net/2445/178745). Although its backend is coded in Python, it is presented in an interactive and modular graphical interface (see figure S1). The software combines the segmentation capabilities of clustering algorithms and the detailed structure description accessed by NLLS fitting routines. The combined use of clustering analysis and NLLS is expected to improve convergence times in problems with several regions of different elemental compositions (e.g., multi-layered structures with different compounds per layer), and might also help the algorithm to converge in pixels classified as spectral outliers (i.e., pixels presenting strong and unique variations in their spectral characteristics in problems with complex multi-component spectra), as they might be previously classified by the clustering algorithms in their own group. The main advantage of combining clustering and NLLS is the fine control it grants to the user over the models fitted, as any given region in the dataset may be tweaked and analysed independently at any time.

In order to validate the software accuracy and capabilities, we will present as a case-example the study of a sample of granular cerium oxide mesoporous material, doped with praseodymium and gadolinium, an ideal showcase of ***WhatEELS*** capabilities, as every tool is utilized for a complete characterization of the cation (elemental) distribution and of the Ce oxidation state in the material.

1.1 WhatEELS. Software architecture

The interactive shell of ***WhatEELS*** is based on **Panel**[36], and **Holoviews**[37]. The current graphical backend is **Bokeh**[38], as it gives access to the plasticity of the JavaScript graphical interfaces and widgets for interactive customization through Python code. It is also interchangeable with **Plotly**[39] and **Matplotlib**[40], provided some minor changes in the source code. Below the surface, the NLLS fitting is based on a library called **lmfit**[41], that expands the **SciPy**[42] fitting capabilities. Finally, the current file loading system relies on **HyperSpy**[35], as it is the most complete tool available to get the information in the standardized dm3 and dm4 formats extracted from the TEM.

A workflow chart for a standard EELS analysis procedure using ***WhatEELS*** is shown in fig.1. The software tool is comprised of two main blocks. (1) The 'core fitting components' block (i.e., the specific tools that carry out the fitting of the spectral datasets and provide an integrated solution for data analysis and results visualization) contains the *model constructor* and the *results* analysis tool, as well as the *pre-analysis*

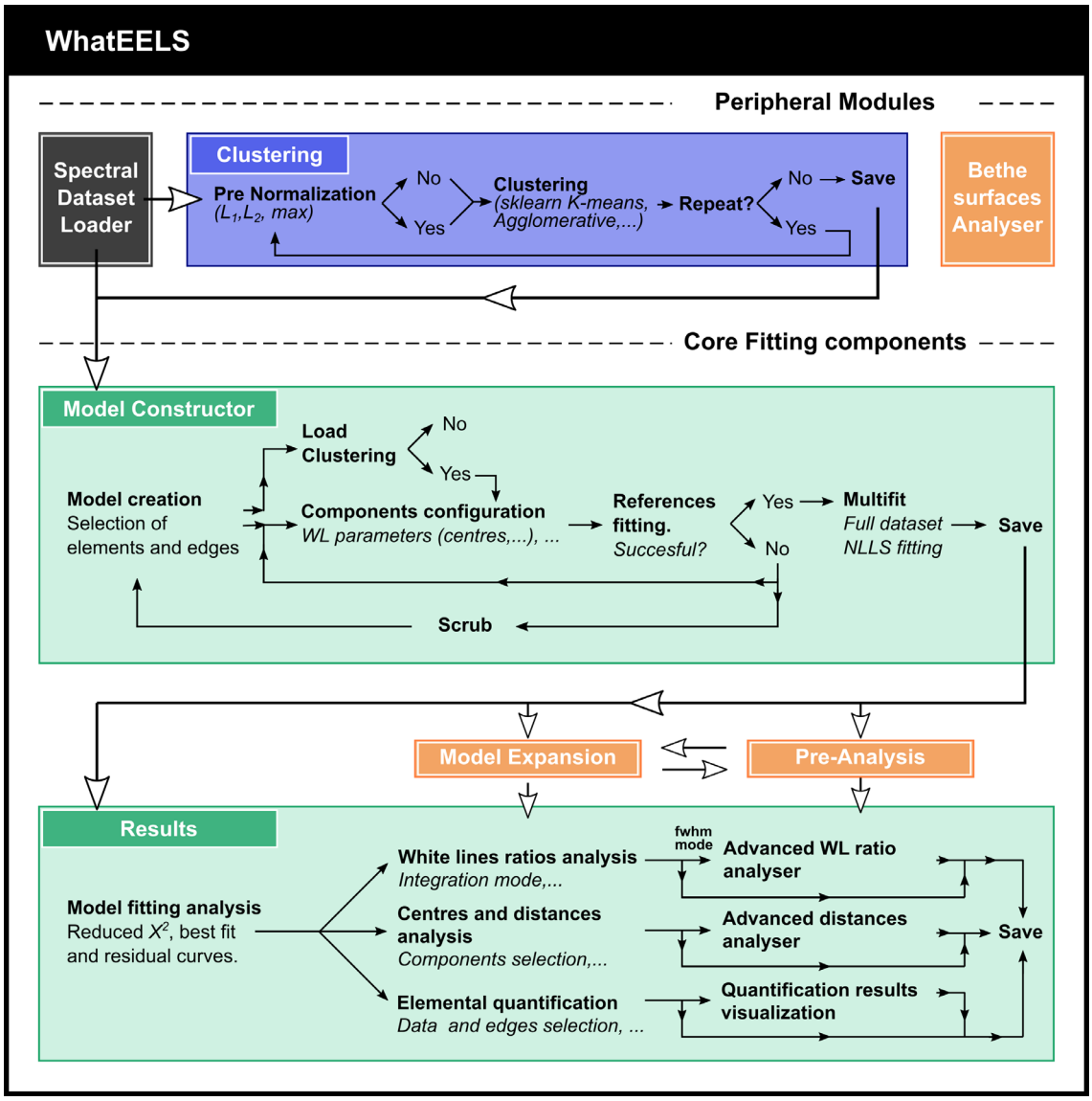

Figure 1. Flow-chart for **WhatEELS**. Each coloured box represents a separated tool. The arrows indicate the chronological progression in a standard EELS data analysis process.

and *model expansion* tools. (2) The 'peripheral modules' block (i.e., all those tools that can be utilized independently and are not necessarily required for the NLLS fitting routines) currently includes the *clustering* analysis tool, the *Bethe-surfaces analyser* tool and the *spectral dataset loader*. The later, although included as part of the peripheral modules, is always the departing point for any EELS dataset analysis utilizing ***WhatEELS***. Notice that the *Bethe-surfaces analyser* (top-right corner) is isolated from the rest of the tools, as it can be used separately at any time and does not demand a loaded dataset. Notice also that the chart is colour-coded. The tools framed in orange add optional functionalities that are not required for the completion of a NLLS fitting and analysis. The tools framed in green are the strictly necessary ones to complete the NLLS fitting and the results analysis using WhatEELS, with the exception of the *spectral dataset loader* that is coloured in black. The *clustering* analysis tool is coloured in blue as, although it belongs to the 'peripheral modules' section, it plays a central role in the new methodology combining clustering and NLLS introduced alongside this software tool. Finally, the arrows indicate the standard chronological tasks-flow to complete the type of analysis described in this work. More information about the specifics of each tool may be found in the quick guide provided with the supplementary materials (figs. S1-12).

As represented in the flow chart from fig.1, the tool presents a completely modular approach, as each of the differentiated sections are self-contained. Hence, it provides a solid ground for future expansions of its capabilities (e.g., adding extra software solutions to the peripheral tools such as a support vector machine classifier described in[43]).

The software is aimed for its use in multiple-spectrum datasets, namely spectrum images (SI) and spectrum lines (SL). Thus, the workflow described below applies to those cases. Nevertheless, a simplified version is automatically launched for single spectrum datasets, which limits some of its functionalities as they are then not required. From here on, whenever we talk about pixels we are refereeing indistinctly to an individual pixel in a SI or in a SL.

The first step of the core fitting components block (NLLS) is the model constructor tool (see fig. S3). It relies on the user to indicate the elemental edges on the sample under analysis. If the selected subshell onset falls outside the energy loss axes, it would not be added to the model. The software will automatically place a set of gaussian curves to represent the fine structure when dealing with M, L or N shells (typically, WLs are the default expected features of the M_{54} and L_{32} subshells in most transition metals and lanthanide oxides). Lorentzian, PseudoVoigt and SplitLorentzian curves are also supported. Furthermore, it will automatically approximate the continuum excitation with curves calculated by integrating the cross-section of the generalized oscillator strength (GOS) surfaces of the database provided according to the bounds imposed by the experimental parameters. If no database is available, some sample curves are included that are automatically selected to fit the continuum depending on the subshell selected. The parameters for these components (e.g., centre, sigma and amplitude of a gaussian curve) are readily available for inspection and modification, as well as their fitting constraints (see fig. S4). An additional tool to create any number of extra components for the elements of the model is also included.

Once the model is created, the user may load a saved clustering segmentation file to divide the dataset accordingly. Each area will be represented by its segmentation map and reference spectra (i.e., the collection of pixels of that area and their channel-average spectra). The default case (i.e., no clustering segmentation areas added)

selects the reference spectra as the average of the whole dataset. Using segmented areas will allow the user to modify the fine structure components independently (i.e., setting initial different parameter values and bounds, and even deleting or blocking them, for each area).

After the values of the parameters and their boundaries are configured for every component in each area, an assessment of the proposed model is carried out by fitting each reference spectrum (all together or individually). This step serves a dual purpose. First, it evaluates the convenience of the elements, parameters and bounds set, as the user gets an initial fitted model result for the reference spectra. Second, when using multiple reference areas, the convergence values for the parameters of each one of their fitted references will be set as the initial state values for the multiple-pixel fitting (MultiFit) process. Hence, the overall fitting convergence times, accuracies and resilience to divergence problems are likely to be improved, given that those pixels groups (resolved via clustering segmentation) are linked by the nature of their spectral features. As this process can be repeated for each area any given number of times, the parameters values and bonds can be configured on the fly and the fitting results for the reference spectra are ready for visual inspection. Thus, iterations with small corrections in place are easily completed, and the workflow is efficient.

The final part of the model constructor tool is the dataset NLLS fitting routine, or MultiFit. To run it, the only requirement is to have previous reference fitting results and selecting the areas to be included (e.g., we may want to leave out areas dominated by background noise, i.e., areas without sample of interest and separated by the clustering algorithm of choice).

The *results analysis* tool becomes available whenever a MultiFit process is completed. It is presented with an initial assessment of the fitting accuracy by means of an interactive mapping image of the reduced chi square ($r.\chi^2$) values and an overlay of graphs of the initial data, best-fit model and residuals per pixel (see fig. S5). From here, 3 analysis tools may be launched: (1) centre-analysis, (2) WL-analysis and (3) element quantification. The first two are an instrumental part of the software for the study of oxidation states and elemental coordination in TM-ox and RE-ox. The quantification tool is an inclusion that follows the Egerton method[9] for quantification. It allows the user to tweak the integrated cross sections by selecting a sharp cut of the surface by a finite beta (β) collection angle (i.e., the finite experimental angle for the collection of electrons in the spectrometer, determined by the physical aperture). It also allows the further correction of the cross section by a geometric factor resulting from the effect of having finite values for the β collection angle and the alpha (α) convergence angle (i.e., the finite experimental angle defined by the convergent electron beam over the sample illuminated with respect to the column axis)[44]. In all of the 3 available tools, an absolute control for the data analysis and results visualization is given to the user (e.g., the integration windows width and position when selecting the WL for the ratios calculations, or for the areas of the spectra selected for integration when quantifying elements).The software also provides a default option which assigns sensible key values (usually computed from the NLLS fitted model and based in our experience) to each of the possible variables of the analysis tools. Moreover, the user is given the choice of changing between raw data and fitted data from the models for integration calculations in the WL-ratio analyser and quantification tool, or even a mixed approach in which part of the fitted data for a specific area may be subtracted from the raw data for the calculations (e.g., subtracting the counts of specific model components from the raw data to carry out quantification when overlapping occurs).

The *pre-analysis* tool provides information on the r.χ^2, the best-fit model and residual curves for each pixel and relative error mappings of the parameters. The *Model-expansion* tool provides an interface to create a second model on top of the first one, with extra components for further refinement. Any of the initially loaded cluster-areas (if any) that were left unfitted can now be completed. It also allows to lock some (or all) of the component's parameters for the second fitting, to speed up convergence even when we are adding extra curves to the mix, and thus increasing the model complexity. They are automatically unlocked whenever a first successful multiple-fitting is completed in the model constructor (optional tools, i.e., non-mandatory to visualize the results).

It is strongly recommended to feed spectra to the model creator tool without background preceding the lowest energy loss edge, as the addition of a power-law component (allowed in the model constructor) usually hampers the performance of the fitting routines. Deconvoluted spectra are always preferred for an accurate fitting of the continuum components (specially in samples with thicker areas, and thus, with a strong multiple scattering contribution to the electron counts after the edge onset).

Moving onto the peripheral modules, the *clustering* tool is an interactive shell programmed on top of the popular scikit-learn[45,46], that currently gives access to 2 different algorithms (K-means and hierarchical-agglomerative clustering) in an easy and visual stylized way. It also allows to decide which pre-normalization step, if any, should be selected. The tool is launched in a single dashboard presenting the clustering algorithm customization options, the results visualization panels and saving options in a single window (see figure S2). This allows a dynamic and iterative data-treatment approach, in which the user can compare the results of several runs with slight modifications of the available parameters and select the one with the best results. The singularities of using different clustering classification algorithms with EELS datasets can be found elsewhere.[20]

The *Bethe-surface analyser* tool can be used to visualize the so-called Bethe surfaces or GOS surfaces of different elements (elemental shells and subshells of those elements are available) and the effects that the experimental parameters have on them: Electron energy (E_0), collection and convergence angles. To do so, it requires a suitable database, since it does not carry out any calculations internally. Initially, it will always try to run on the files associated provided by the DM suite (looking for them in the directories that they are typically installed in the old versions of DM, and alternatively in a directory provided by the user). It can always be fed by other databases, as long as they respect the format of the old DM ones. The Bethe-surface analyser is a convenient tool to prepare in advance the experiments since it shows the possible effects that a specific combination of finite collection and convergence angles will have on the acquired spectra beforehand.

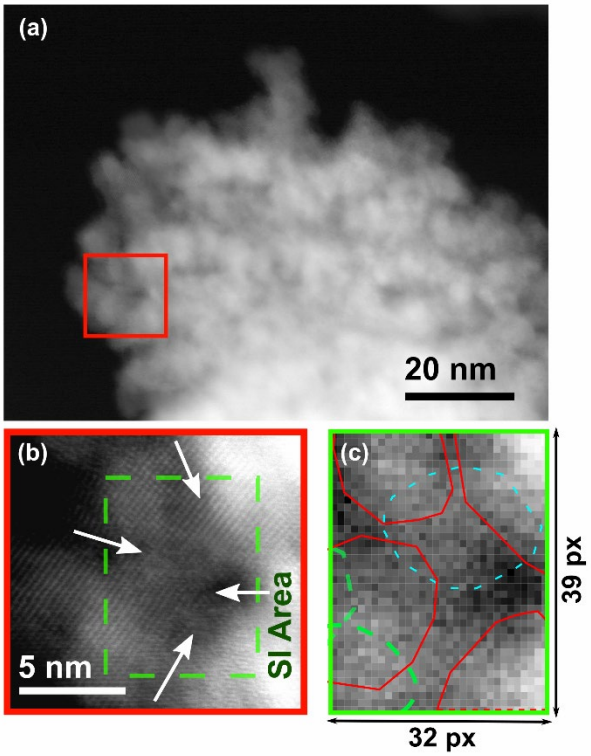

Figure 2. (a) HAADF low resolution image of the collapsed granular mesoporous structure of CeO_2. (b) High resolution HAADF image of the zoomed area marked in (a) with a red square. The arrows indicate the direction of the possible grain boundaries. (c) Co-acquired EELS signal intensity mapping, with a schematic of the proposed grain structure overlayed on top.

The use of any of these tools is not required to attain a successful fit by NLLS, thus they are classified as peripheral modules. Nevertheless, it is precisely the use of clustering and NLLS as a unit what makes ***WhatEELS*** so appealing for complex fitting problems, as we will demonstrate later.

2. Materials and Methods

A sample of granular mesoporous CeO_2 doped with Pr and Gd is used as the test sample. It has the following expected stoichiometry: $Ce_{0.8}O_2Pr_{0.1}Gd_{0.1}$ (CGPO). It was synthesized from a Kit-6 silica template, with a dual set of channels describing each a gyroidal surface. Further details about the synthesis and characterisation of the material and its applications may be found elsewhere[34], and a detailed scheme of the actual mesoporous morphology is also described in the ***supplementary materials*** (fig. S13 and S14). The mesoporous granular material is expected to show a Ce^{4+} to Ce^{3+} reduction and a Pr/Gd dopant segregation towards grain boundaries (GB) and grain surfaces (GS), as has been already reported in the literature for similar materials[47,48], and demonstrated elsewhere in this particular case[34].

Although the mesoporous structures in this sample were expected to have a double-gyroidal interpenetrated morphology, the dataset we present here corresponds to a region in a mesoporous structure with an apparent collapse of the channels (see fig. 2a and fig. S15 in the supplementary materials). The cation reduction and dopant segregation are however unaffected by this collapse of the long-range structure[34],

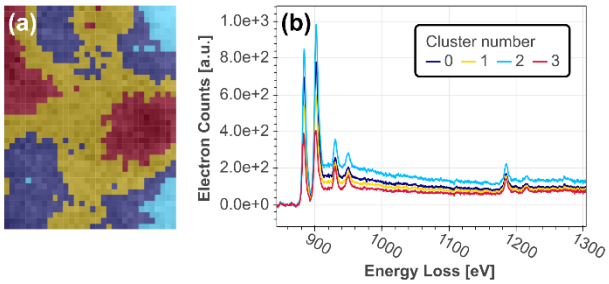

Figure 3. (a) Overlay of the SI and the clustering label map resolved by the K-means clustering algorithm applied on the raw dataset. b) Reference signals for each of the clusters.

and thus, it is the multiple grains and grain boundaries in a relatively homogeneous thin area over an empty TEM grid hole what makes this dataset so appealing to demonstrate ***WhatEELS***. The positions of the grain boundaries are included as part of fig. 2b, and the schematics of the possible grain structure and the co-acquired mapping for the EELS dataset signal (with the pixel granularity for the SI) are shown in fig. 2c (c.f., supplementary material, fig. S15).

The high angle annular dark field (HAADF) images and the EELS SI were acquired in a JEOL-ARM at 200keV. The spectrometer collection angle was 41.67 mrad and a 25 mrad convergence angle was selected for the spectral acquisition.

The dataset was subjected to a denoising treatment via PCA and the Ce edge onset background was removed using HyperSpy, previous to its introduction in ***WhatEELS***.

3. Results

To illustrate the usefulness of ***WhatEELS*** software, in this section the different tools will be applied to unveil the chemical configuration of this granular CGPO mesoporous material, with special attention to Ce oxidation state and Pr and Gd dopant distribution within the mesoporous structure. The overall format of the graphs and mappings shown in this section is almost identical to the ones in the ***WhatEELS*** graphical interface software (c.f., supplementary figures S1 to S12), so we have a faithful representation of what we might encounter using the software with any other dataset.

The results of the segmentation via clustering analysis are shown in fig. 3. In this case, we selected 4 clusters as the target number for the K-means algorithm. Even though the spectral background was subtracted beforehand, the segmentation appears to be dominated by thickness effects, as the clusters appear to be mainly separated by this factor. In any case, comparing the relative intensities of the elemental WL (CeM_{54} 883-901 eV, PrM_{54} 931-951 eV and GdM_{54} 1185-1217 eV) we already have a qualitative observation that hints towards a possible relative increment of the dopants towards grain surfaces (GS) and boundaries (GB) (cluster 3 signal, in red, in fig. 3b).

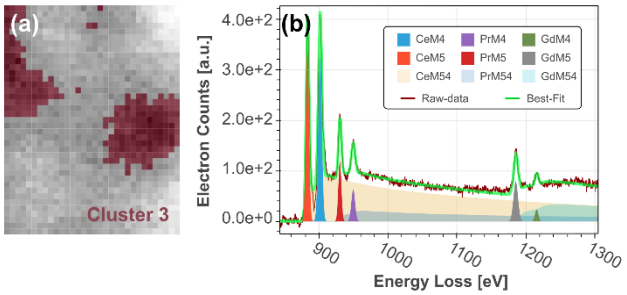

Figure 4. (a) Overlay of the SI area and the cluster 3 area resolved by K-means. (b) Overlay of components for the initial fit of the model for the reference spectrum of the cluster 3.

The model was automatically created for the whole sample after selecting the elements and their specific edges. We only introduced small variations in the gaussian centres for the Ce ELNES components in each of the segmented areas (as we already observe that in some of them a chemical shift may be occurring). In fig. 4 we show the results of the initial fit for the reference spectrum of the area labelled as cluster-3 (red in fig. 4a), separated previously by the K-Means algorithm (fig. 3). This segmented area is populated by several GB and GS (fig. 2b,c). The curves with shadowed areas in the spectra of fig. 4b correspond to the individual components that give shape to the included edges (ELNES gaussian curves and integrated cross sections for the continuum of the CeM_{54}, PrM_{54} and GdM_{54} edges). The green line is the sum of all the components and is called the best-fit curve of the fitted model.

Once a satisfactory (qualitative evaluation) initial fit was in place for each area

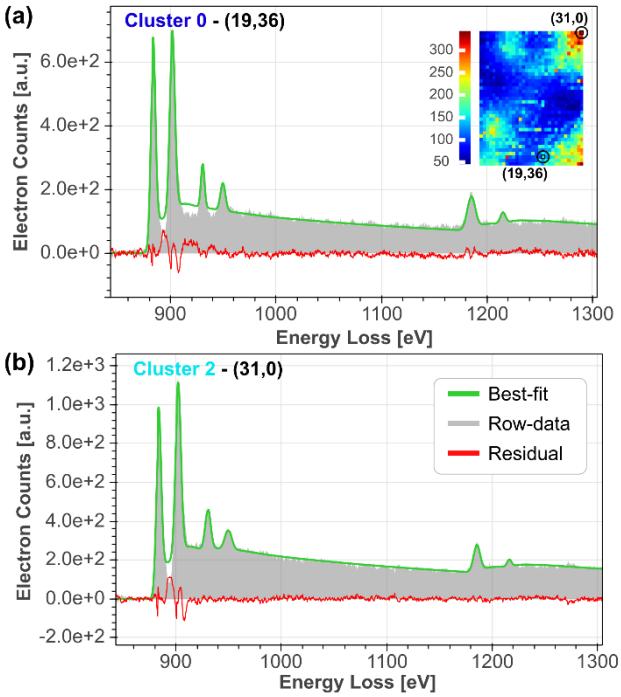

Figure 5 Best-fit model, residual curve and raw data for two different pixels in two different clusters, after the MultiFit was carried out. On the inset, an image of the r.χ^2 values mappings.

reference signal, the MultiFit routine was called for the whole dataset selecting the 4 clusters separately. This way, the model fitting for each cluster is initialized close to its reference spectrum, and the subsequent fitting process in each pixel is more likely to converge faster (c.f. fig. S16).

In fig. 5 we show the resulting r.χ^2 mapping (inset), which is often used as the main indicator to evaluate the goodness for a given NLLS fitting result. We also include a graphical interface that shows an overlay of the original raw-data, the best-fit curve and the residual curve (i.e., difference between the raw-data and the best-fit), dynamically linked with the r.χ^2 mappings for each pixel (i.e., selecting a specific pixel in the map changes the set of graphics shown). This feature is not only complementary to having the values for the r.χ^2, but in some cases fundamental to understand the real accuracy of the fitting. One example is shown in fig. 5, as we include the curves-overlays for two different pixels. The pixel (19,36) in fig. 5a presents a value of reduced χ^2 is 163.905, and for (31,0) in fig. 5b the reduced χ^2 is 330,963. Nevertheless, if playing close attention to the best-fit model curves (green) and the original raw data (area shaded in grey) a higher deviation between curves for the (19,36) pixel in the spectrum area ranging from 910 to 925 eV (between Ce and Pr WLs) is apparent. This contradiction can be explained by analysing the behaviour of the fitted model between both CeM_{54} WLs (from 883 to 901 eV). The NLLS algorithm is unable to reconcile the proposed combination of integrated cross section (continuum) and gaussian (WLs) curves with the actual experimental electron counts in this portion of the spectra throughout the whole area of the spectrum image. This limitation finally results in a positive biased r.χ^2 value in every single pixel. However, the bias weight is not the same for every single spectrum from the SI fitted. The thicker areas in the sample (thus, with higher values of electron counts) present a larger separation between the fitted model and the experimental counts. As the r.χ^2 is computed from the non-normalized differences between the raw data and the fitted model, those thicker regions will present the higher degree of positive bias for the r.χ^2. Precisely for this dataset, this positive bias outweighs any other contribution to the r.χ^2. This exposes the dangers of blindly trusting in the r.χ^2 as the single indicator of fitting goodness in NLLS, and we always recommend a further analysis of the residual curves (and if possible, the relative error mappings in the *pre-analysis* tool) to validate the NLLS fitting results.

Once the NLLS fitting results have been evaluated one may move onto the analysis of the data structures that will provide information about the oxidation states and elemental distribution. A reduction of cerium from Ce^{4+} to Ce^{3+} can be observed as a chemical shift of the $M_{5,4}$ energy loss onset from 884 to 881,4 eV in EELS[7,49]. Hence, it may be resolved by an analysis of the central position of the gaussian curves fitted to the WL in the energy onset by NLLS, using the centre and distances analysis tool. This tool extracts from the fitting results the centre values for the peak-like curves for the ELNES, if any is available, and the onset values for the continuum curves. It has been sometimes favoured in the literature the comparison of the feature of interest with a fixed feature on the spectrum (e.g., CrL_3 WL and OK onset[33]), over the evaluation of a single energy loss value. This dampens the effects of artifacts introduced by beam instabilities when acquiring the spectra, as any random and local energy shift may easily be mistaken for an actual chemical shift with physical meaning. Fig. 6a,b and c show the heatmaps for the Ce and Gd M_5 WL centres and the absolute distance difference between them. A clear texture on the CeM_5 mapping is visible, whereas the GdM_5 is almost flat. The CeM_5 modulation is, thus, translated into the distances-map. When dealing with SI, the tool allows to draw lines in specific locations to generate scatter graphs for the parameters selected for further local analysis. Fig. 6d contains a

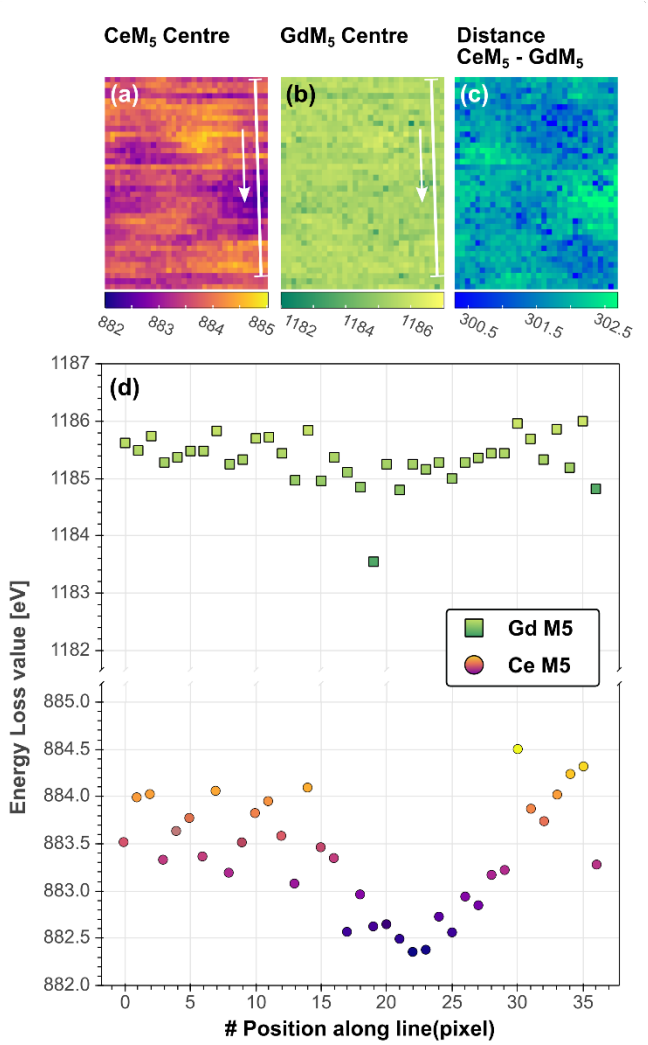

Figure 6 Heatmaps of the gaussian centre values for the CeM_5 (a), GdM_5 (b) and the absolute difference between them(c). (d) Broken graph (energy loss axis) to show the centre values for the pixels along the lines shown in the heatmaps, traversing a GB.

panel constructed with these graphs (c.f., fig. S7) for the line traversing a GB (see fig. 2b,c) indicated in the heatmaps with lines. A clear chemical shift of the CeM_5 towards lower energy loss values is observable at the GB. In the literature, this type of displacement in the energy axis is associated with a change in the cerium oxidation state from 4^+ to 3^+. Meanwhile, an almost flat distribution around 1185.5 eV for the GdM_5 WL centre is observable, which is our fixed feature in this example. These results are the first solid prove for the hypothesis of Ce reduction when traversing GB and in GS in our sample.

As a crosschecking measure, we launched the WL ratio analyser tool. Usually, integration of the WL intensity values for a given energy range is preferred over single energy loss channel evaluations to mitigate noise effects. In fact, in the literature the differences in the WL ratios and their relationship with changes in the oxidation states are often given for a specific integration range[7,50].

A powerful tool is included in the ***WhatEELS*** WL ratio analyser to face the possibility of not knowing a priori the correct parameters for the integration ranges, or even to check the validity of the values in the literature. The tool carries out a systematic calculation of

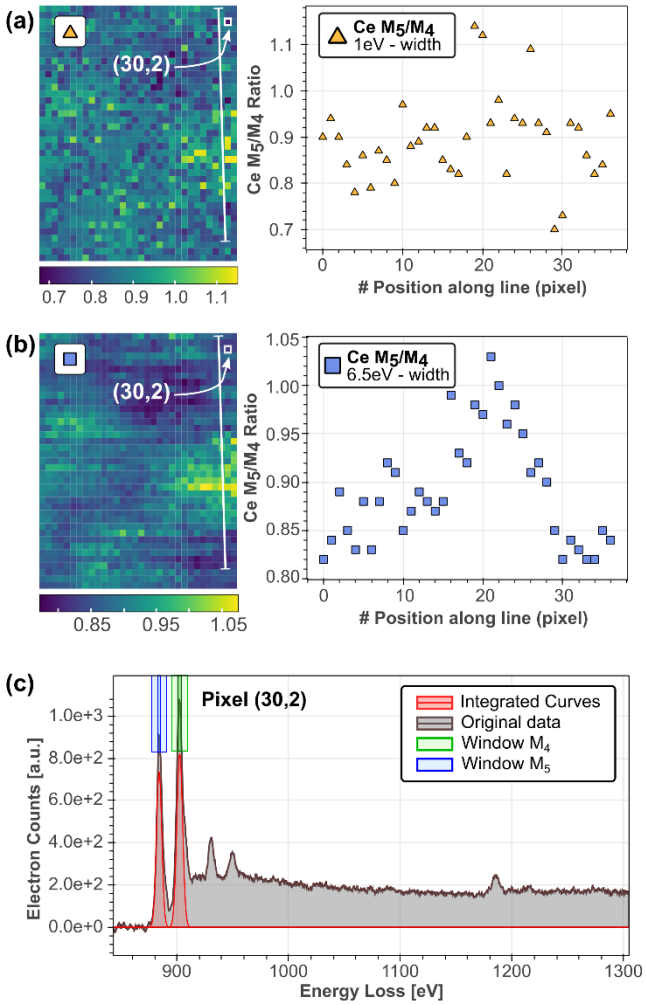

Figure 7. (a) Heatmap and scatter plot for the pixels along the white line for the Ce M5/M4 WL ratio with an integration window of 1eV. (b) Heatmap and scatter plot for the pixels along the white line for the Ce M5/M4 WL ratio with an integration window of 6.5eV. (c) Overlay of the raw data, the WL data integrated (fitted model) and window ranges (1 and 6.5eV) for the pixel (30,2) marked in (a) and (b).

WL ratios of the selected components for several integration ranges, which are calculated multiplying the sigma value of the corresponding WL, at each pixel, by a list of factors (see fig. S8 and S9). The utility of this routine is clearly illustrated in fig. 7. When selecting a narrow range (fig. 7a), the resulting WL-ratio heatmap is noisy, and no clear structure can be discerned. Using this result to get the ratio across the same GB as before, one might conclude that no clear signs of spatially resolved elemental reduction were found (yellow triangles graph). Nevertheless, when selecting an appropriate integration width (6.5 eV, fig. 7b), the heatmap recovers the same structure observed in the centre analysis tool for the CeM_5. Furthermore, the M_5/M_4 ratio shows a clear increment traversing the GB, confirming the Ce reduction towards GB and GS, and in good agreement with the literature values given for the Ce WL ratios for the expected oxidation states[10,51]. In this particular case, we decided to integrate the fitted gaussian curves (red curves in fig. 7c) for the WL ratios, excluding the values of the continuum excitation as we saw in the residual and $r.\chi^2$ analysis (fig. 5) that they were a clear contributor to the overestimation of the best-fit model in energy range between the CeM_{54} WLs.

Finally, the quantification tool was used to get a result for the elemental distribution, and the results are shown in fig. 8. An integration range width of 45eV was selected manually, beginning at the energy loss value of the elemental onsets, for every pixel in the SI (information extracted from the components of the best-fit model). The same integration window width was selected for all 3 elements. The integrated intensity was calculated using the raw data, given the persistent overestimation of the electron counts in the best-fit model between the Ce WLs pointed out previously (fig. 5). Nevertheless, to get each of the elemental integrated intensities the electron counts corresponding to the rest of the elements (calculated by NLLS fitting) were subtracted. This strategy improves the consistency for the Pr integrated intensities, avoiding the background subtraction computation in the PrM_{54} onset which is heavily influenced by the proximity of the $CeM_{5,4}$ edge. The option of extra corrections was also activated and applied to the $GdM_{5,4}$ edge, as the commonly ignored CeM_{32} minor edge (onset at 1185 eV, same as the GdM_{54}) appeared to be responsible for an overestimation of the Gd integrated intensity (see fig. S11 and S12). These extra corrections consist of a simple calculation of the ratio between the integrated cross section of the major edge selected (CeM_{54}) and the minor edge under consideration (CeM_{32}), for the given values of collection and convergence angles and incident electrons energy. Then, the intensity for the minor edge (CeM_{32}) is calculated by multiplying the ratio and the measured integrated intensity of the corresponding major edge (CeM_{54}). Finally, the newly calculated integrated intensity (CeM_{32}) is subtracted from the measured integrated intensity of the affected edge (GdM_{54}). All these options are customizable directly on the application panel (see fig. S10). An increment of the dopant ratio towards GB and GS is observable in fig. 8a,b, coinciding with the areas of Ce reduction observed in figs. 6,7. It is also noticeable in the scatter plot graph (fig. 8c) that the ratios calculated with the corrections in place get closer to the expected stoichiometric values towards the

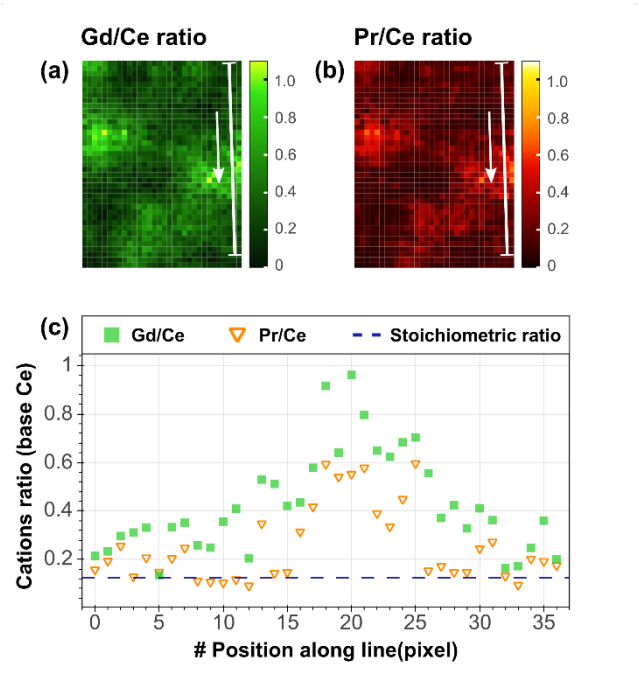

Figure 8 Heatmaps of the relative ratio compositions of Gd (a), in green, and Pr (b), in red, with respect to Ce. (c) Scatter plot of the relative ratios of Gd / Ce and Pr / Ce along the line of pixels marked over the heatmaps. The stoichiometric expected value for both elements' ratios, 0.125, is marked as the dashed blue line.

bulk regions of the CeO_2 grains. The slight overestimation can be attributed to the intricated structure of the mesoporous material, as the effects of multiple overlapping grains in the real 3D structure are probably affecting the conventional planar EELS SI acquired, a 2D projection image (see fig. 2b,c).

4. Discussion

The doped granular CGPO mesoporous material provided a challenging EELS dataset for analysis due to the proximity between the CeM_{54} WL and PrM_{54}, and the edge overlapping problems between CeM_{32} and GdM_{54}. Hence, the good results obtained for spatially resolved distribution of Ce oxidation states and the Pr/Gd dopant elemental quantification demonstrate the large potential of ***WhatEELS*** as a software solution for advance nanomaterials characterization through TEM EELS experiments.

Notably, any nanomaterial or device composed by transition metal oxides (TM-ox) and rare earth oxides (RE-ox) constitutes a good candidate for analysis using ***WhatEELS***, as they usually present characteristic ELNES features directly related to fundamental nanoscale physics (e.g., cation/anion oxidation states) and, thus, linked to the macroscopic properties and specific performances measured (e.g., conductivity and reaction rates). TM-ox and RE-ox can be found in applications in a wide variety of fields, aside from mixed ionic-electronic conductors (MIEC) for solid oxide fuel cells (SOFC) and solid oxide electrolyser cells (SOEC)[34,52,53]. For example, in improved photocatalytic devices and processes for hydrogen production via water splitting[54,55] and electrocatalytic devices for improved hydrogen evolution reactions[56] in the field of new energy production and storage solutions. Also, in the fields of materials research for environmental applications, such as catalytic mediums for volatile organic compounds capture[57] and methane total combustion[58], and even in multifunctional materials that exhibit photocatalytic properties for benzene degradation process and photochromatic properties for photoelectronic applications[59]. More notably yet, in the field of nanomagnetic materials the characterization through EELS analysis presents a great opening for the ***WhatEELS*** software solution, given the general elemental composition of these materials (i.e., iron and nickel oxides, mixed with other TM-ox) and the importance of resolving properties such as the local oxidation state or cationic inversion ratio accurately.[60,61]

5. Conclusions

In this work we present a new software tool, ***WhatEELS***, designed specifically with the purpose of analysing multiple pixel EELS datasets (SI) by combining the power of clustering algorithms for image segmentation and NLLS fitting routines to make the most of the spectral features near the edge onset. The tool was born from the necessity we often encountered of an improved workflow efficiency when dealing with these types of problems.

The interactive solution is based on Panel, a library with an ongoing support from the creators that launches reactive dashboards using as backend any of the major web browsers (e.g., Google Chrome, Mozilla Firefox), which in principle would enable any operative system with a Python interpreter to use ***WhatEELS***. Furthermore, its modular construction leaves room for further software expansions down the line.

We presented and described the full characterization process using ***WhatEELS*** for a test sample of CGPO, where we sought to investigate possible changes in the Ce oxidation state and inhomogeneous dopant distributions. The results revealed localized

reduction of Ce^{4+} to Ce^{3+} in different areas of the sample (showing coherent results via 2 different characterization methods, WL ratios and WL centre positions) and segregation of dopants towards GB and GS (via the included Egerton quantification method). This test demonstrated the potential of this tool when dealing with problems of similar nature via ELNES analysis of EELS SI. Furthermore, this initial assessment of the inner workings of the proposed clustering – NLLS combination hinted to a possible improvement in the convergence times over the default option of a non-segmented SI (i.e., the classic approach of fitting the whole image area in bulk), although more work and tests will be required to identify the optimum number of clusters configuration and the type of samples that can potentially be benefited by higher fitting times when following this methodology.

Finally, the open-source nature of ***WhatEELS*** and the little programming knowledge required may be of benefit to a large number of entry-level researchers and students beginning their path on EELS data analysis for materials science.

Acknowledgements

The authors acknowledge the financial support from the Spanish Ministery of Science and Innovation (MICINN) through the project PID2019-106165GB-C21, the Spanish Research Network RED2018-102609-T, and the FI-AGAUR Research Fellowship Program, Generalitat de Catalunya (FI grant 2018FI_B_00360). They also acknowledge the financial support of the 'Generalitat de Catalunya' (2017 SGR 1421, NANOEN) and MITECO for the financial support of the project 3DPASSION (PID2019-107106RB-C3119S01452-006). Finally, the authors acknowledge the use of instrumentation as well as the technical advice provided by the National Facility ELECMI ICTS, at DME-UCA and UMEAP-UB nodes, and the use of instrumentation in the NanoBioMedical Centre of the Adam Mickiewicz University in Poznan backed by the technical advice of Dr. Emerson Coy and Professor Stefan Jurga.

References

[1] D.B. Williams, C.B. Carter, The Transmission Electron Microscope, in: Transm. Electron Microsc., Springer US, Boston, MA, 1996: pp. 3–17. https://doi.org/10.1007/978-1-4757-2519-3_1.

[2] N.D. Browning, D.J. Wallis, P.D. Nellist, S.J. Pennycook, EELS in the STEM: Determination of materials properties on the atomic scale, Micron. 28 (1997) 333–348. https://doi.org/10.1016/S0968-4328(97)00033-4.

[3] C. Colliex, D. Ugarte, Z.L. Wang, M. Gasgnier, V. Paul-Boncour, High spatial resolution analytical electron microscopy studies on the Co/CeO2 system, Surf. Interface Anal. 12 (1988) 3–10. https://doi.org/10.1002/sia.740120104.

[4] P. Cueva, R. Hovden, J.A. Mundy, H.L. Xin, D.A. Muller, Data processing for atomic resolution electron energy loss spectroscopy, Microsc. Microanal. 18 (2012) 667–675. https://doi.org/10.1017/S1431927612000244.

[5] K. Kimoto, T. Asaka, T. Nagai, M. Saito, Y. Matsui, K. Ishizuka, Element-selective imaging of atomic columns in a crystal using STEM and EELS, Nature. 450 (2007) 702–704. https://doi.org/10.1038/nature06352.

[6] M. Haruta, H. Higuchi, T. Nemoto, H. Kurata, Local quantification of coordination number for perovskite-related oxides using atomic resolution EELS maps, Appl. Phys. Lett. 113 (2018). https://doi.org/10.1063/1.5041063.

[7] L.A.J. Garvie, P.R. Buseck, Determination of Ce4+/Ce3+ in electron-beam-damaged CeO2 by electron energy-loss spectroscopy, J. Phys. Chem. Solids. 60 (1999) 1943–1947. https://doi.org/10.1016/S0022-3697(99)00218-8.

[8] H. Tan, J. Verbeeck, A. Abakumov, G. Van Tendeloo, Oxidation state and chemical shift investigation in transition metal oxides by EELS, Ultramicroscopy. 116 (2012) 24–33. https://doi.org/10.1016/j.ultramic.2012.03.002.

[9] R.F. Egerton, Electron energy-loss spectroscopy in the electron microscope, Springer, 2011.

[10] T. Manoubi, C. Colliex, P. Rez, Quantitative electron energy loss spectroscopy on M45 edges in rare earth oxides, J. Electron Spectros. Relat. Phenomena. 50 (1990) 1–18. https://doi.org/10.1016/0368-2048(90)80001-Q.

[11] F. Hofer, B. Luo, Towards a practical method for EELS quantification, Ultramicroscopy. 38 (1991) 159–167. https://doi.org/https://doi.org/10.1016/0304-3991(91)90117-O.

[12] S. Estradé, L. Yedra, A. López-Ortega, M. Estrader, G. Salazar-Alvarez, M.D. Baró, J. Nogués, F. Peiró, Distinguishing the core from the shell in MnO x/MnO y and FeO x/MnO x core/shell nanoparticles through quantitative electron energy loss spectroscopy (EELS) analysis, Micron. 43 (2012) 30–36. https://doi.org/10.1016/j.micron.2011.04.002.

[13] N. Bonnet, N. Brun, C. Colliex, Ultramicroscopy_1999_Bonnet, 77 (1999) 1–16. papers2://publication/uuid/4B51D76C-A75D-4DF3-827F-3C7F52AE0225.

[14] N. Bonnet, D. Nuzillard, Independent component analysis: A new possibility for analysing series of electron energy loss spectra, Ultramicroscopy. 102 (2005) 327–337. https://doi.org/10.1016/j.ultramic.2004.11.003.

[15] M. Bosman, M. Watanabe, D.T.L. Alexander, V.J. Keast, Mapping chemical and bonding information using multivariate analysis of electron energy-loss spectrum

images, Ultramicroscopy. 106 (2006) 1024–1032. https://doi.org/10.1016/j.ultramic.2006.04.016.

[16] N. Dobigeon, N. Brun, Spectral mixture analysis of EELS spectrum-images, Ultramicroscopy. 120 (2012) 25–34. https://doi.org/10.1016/J.ULTRAMIC.2012.05.006.

[17] S. Lichtert, J. Verbeeck, Statistical consequences of applying a PCA noise filter on EELS spectrum images, Ultramicroscopy. 125 (2013) 35–42. https://doi.org/10.1016/j.ultramic.2012.10.001.

[18] P. Potapov, On the loss of information in PCA of spectrum-images, Ultramicroscopy. 182 (2017) 191–194. https://doi.org/10.1016/j.ultramic.2017.06.023.

[19] P. Potapov, Why Principal Component Analysis of STEM spectrum-images results in “abstract”, uninterpretable loadings?, Ultramicroscopy. 160 (2016) 197–212. https://doi.org/10.1016/j.ultramic.2015.10.020.

[20] P. Torruella, M. Estrader, A. López-Ortega, M.D. Baró, M. Varela, F. Peiró, S. Estradé, Clustering analysis strategies for electron energy loss spectroscopy (EELS), Ultramicroscopy. 185 (2018) 42–48. https://doi.org/10.1016/J.ULTRAMIC.2017.11.010.

[21] R.D. Leapman, C.R. Swyt, Separation of overlapping core edges in electron energy loss spectra by multiple-least-squares fitting, Ultramicroscopy. 26 (1988) 393–403. https://doi.org/https://doi.org/10.1016/0304-3991(88)90239-2.

[22] H. Shuman, A.P. Somlyo, Electron energy loss analysis of near-trace-element concentrations of calcium, Ultramicroscopy. 21 (1987) 23–32. https://doi.org/https://doi.org/10.1016/0304-3991(87)90004-0.

[23] R. Door, D. Gängler, Multiple least-squares fitting for quantitative electron energy-loss spectroscopy - an experimental investigation using standard specimens, Ultramicroscopy. 58 (1995) 197–210. https://doi.org/10.1016/0304-3991(94)00198-V.

[24] K. Riegler, G. Kothleitner, EELS detection limits revisited: Ruby - a case study, Ultramicroscopy. 110 (2010) 1004–1013. https://doi.org/10.1016/j.ultramic.2010.02.010.

[25] M.-T. Chang, R.-F. Cai, C.-C. Chen, S.-C. Lo, Development of Clustering Algorithm Applied for the EELS Analysis of Advanced Devices, Microsc. Microanal. 26 (2020) 2112–2114. https://doi.org/10.1017/s1431927620020486.

[26] Y. Wang, M.R.S. Huang, U. Salzberger, K. Hahn, W. Sigle, P.A. van Aken, Towards atomically resolved EELS elemental and fine structure mapping via multi-frame and energy-offset correction spectroscopy, Ultramicroscopy. 184 (2018) 98–105. https://doi.org/10.1016/j.ultramic.2017.10.014.

[27] T. Akita, N. Taguchi, Practical analysis of Li distribution by EELS, Surf. Interface Anal. 48 (2016) 1226–1230. https://doi.org/10.1002/sia.6082.

[28] X. Mu, A. Kobler, D. Wang, V.S.K. Chakravadhanula, S. Schlabach, D. V. Szabó, P. Norby, C. Kübel, Comprehensive analysis of TEM methods for LiFePO4/FePO4 phase mapping: spectroscopic techniques (EFTEM, STEM-EELS) and STEM diffraction techniques (ACOM-TEM), Ultramicroscopy. 170 (2016) 10–18. https://doi.org/10.1016/j.ultramic.2016.07.009.

[29] L. Yedra, E. Xuriguera, M. Estrader, A. López-Ortega, M.D. Baró, J. Nogués, M.

Roldan, S. Estradé, F. Peiró, Oxide Wizard: An EELS Application to Characterize the White Lines of Transition Metal Edges, Microsc. Microanal. 20 (2014) 698–705. https://doi.org/10.1017/S1431927614000440.

[30] R.D. Leapman, L.A. Grunes, P.L. Fejes, Study of the L23 edges in the 3d transition metals and their oxides by electron-energy-loss spectroscopy with comparisons to theory, Phys. Rev. B. 26 (1982) 614–635. https://doi.org/10.1103/PhysRevB.26.614.

[31] P.A. Van Aken, B. Liebscher, V.J. Styrsa, Quantitative determination of iron oxidation states in minerals using Fe L2,3-edge electron energy-loss near-edge structure spectroscopy, Phys. Chem. Miner. 25 (1998) 323–327. https://doi.org/10.1007/s002690050122.

[32] T. Riedl, T. Gemming, K. Wetzig, Extraction of EELS white-line intensities of manganese compounds: Methods, accuracy, and valence sensitivity, Ultramicroscopy. 106 (2006) 284–291. https://doi.org/10.1016/j.ultramic.2005.09.002.

[33] Á.M. Arévalo-López, M.Á. Alario-Franco, Reliable method for determining the oxidation state in chromium oxides, Inorg. Chem. 48 (2009) 11843–11846. https://doi.org/10.1021/ic901887y.

[34] F. Baiutti, J.B. Portals, S. Anelli, P. Torruella, J.J. Calvino, Tailoring the transport properties of mesoporous doped cerium oxide for energy applications, *Reviewing process.* in *J. Phys. Chem. C.* (n.d.).

[35] E.P. Francisco de la Peña Vidar Tonaas Fauske, Pierre Burdet, Petras Jokubauskas, Magnus Nord, … Andreas Garmannslund, hyperspy/hyperspy: HyperSpy v1.5.2, (2019). https://doi.org/10.5281/zenodo.3396791.

[36] P. Rudiger, X. Artusi, J.A. Bednar, M.S. Madsen, C. B, J. Signell, J.-L. Stevens, M. Liquet, Hoxbro, J. Mease, Andrew, Arne, M. Paprocki, kbowen, E. Jung, H.-Y. Amanieu, J. Winkelmann, L. Talirz, P. A, A. Randelhoff, B. Sullivan, J. Barhak, N. Ghenzi, hoseppan, kleavor, miliante, R. Mulpuri, G. Bischof, A. Thorve, holoviz/panel: Version 0.11.0, (2021). https://doi.org/10.5281/ZENODO.4573728.

[37] P. Rudiger, J.-L. Stevens, J.A. Bednar, B. Nijholt, J. Mease, Andrew, C. B, A. Randelhoff, V. Tenner, maxalbert, M. Kaiser, ea42gh, J. Samuels, stonebig, K. Pevey, F. LB, A. Tolmie, D. Stephan, Hoxbro, J. Bois, S. Lowe, J. Bampton, henriqueribeiro, ruoyu0088, I. Lustig, A. Klein, B. Van de Ven, J. Signell, L. Talirz, L. Barth, holoviz/holoviews: Version 1.14.2, (2021). https://doi.org/10.5281/ZENODO.4581995.

[38] B.V. de V.P.E.M.Z.D.A. Brendan Collins, Bokeh: Essential Open Source Tools for Science, (2020). https://doi.org/10.5281/ZENODO.4317718.

[39] P.T. Inc., Collaborative data science, (2015). https://plot.ly.

[40] T.A. Caswell, M. Droettboom, A. Lee, E.S. de Andrade, J. Hunter, T. Hoffmann, E. Firing, J. Klymak, D. Stansby, N. Varoquaux, J.H. Nielsen, B. Root, R. May, P. Elson, J.K. Seppänen, D. Dale, J.-J. Lee, D. McDougall, A. Straw, P. Hobson, C. Gohlke, T.S. Yu, E. Ma, hannah, A.F. Vincent, S. Silvester, C. Moad, N. Kniazev, E. Ernest, P. Ivanov, matplotlib/matplotlib: REL: v3.4.1, (2021). https://doi.org/10.5281/ZENODO.4649959.

[41] M. Newville, R. Otten, A. Nelson, A. Ingargiola, T. Stensitzki, D. Allan, A. Fox, F. Carter, Michał, D. Pustakhod, lneuhaus, S. Weigand, R. Osborn, Glenn, C. Deil,

Mark, A.L.R. Hansen, G. Pasquevich, L. Foks, N. Zobrist, O. Frost, A. Beelen, Stuermer, kwertyops, A. Polloreno, S. Caldwell, A. Almarza, A. Persaud, B. Gamari, B.F. Maier, lmfit/lmfit-py 1.0.2, (2021). https://doi.org/10.5281/ZENODO.4516651.

[42] P. Virtanen, R. Gommers, T.E. Oliphant, M. Haberland, T. Reddy, D. Cournapeau, E. Burovski, P. Peterson, W. Weckesser, J. Bright, S.J. van der Walt, M. Brett, J. Wilson, K.J. Millman, N. Mayorov, A.R.J. Nelson, E. Jones, R. Kern, E. Larson, C.J. Carey, İ. Polat, Y. Feng, E.W. Moore, J. VanderPlas, D. Laxalde, J. Perktold, R. Cimrman, I. Henriksen, E.A. Quintero, C.R. Harris, A.M. Archibald, A.H. Ribeiro, F. Pedregosa, P. van Mulbregt, A. Vijaykumar, A. Pietro Bardelli, A. Rothberg, A. Hilboll, A. Kloeckner, A. Scopatz, A. Lee, A. Rokem, C.N. Woods, C. Fulton, C. Masson, C. Häggström, C. Fitzgerald, D.A. Nicholson, D.R. Hagen, D. V. Pasechnik, E. Olivetti, E. Martin, E. Wieser, F. Silva, F. Lenders, F. Wilhelm, G. Young, G.A. Price, G.L. Ingold, G.E. Allen, G.R. Lee, H. Audren, I. Probst, J.P. Dietrich, J. Silterra, J.T. Webber, J. Slavič, J. Nothman, J. Buchner, J. Kulick, J.L. Schönberger, J.V. de Miranda Cardoso, J. Reimer, J. Harrington, J.L.C. Rodríguez, J. Nunez-Iglesias, J. Kuczynski, K. Tritz, M. Thoma, M. Newville, M. Kümmerer, M. Bolingbroke, M. Tartre, M. Pak, N.J. Smith, N. Nowaczyk, N. Shebanov, O. Pavlyk, P.A. Brodtkorb, P. Lee, R.T. McGibbon, R. Feldbauer, S. Lewis, S. Tygier, S. Sievert, S. Vigna, S. Peterson, S. More, T. Pudlik, T. Oshima, T.J. Pingel, T.P. Robitaille, T. Spura, T.R. Jones, T. Cera, T. Leslie, T. Zito, T. Krauss, U. Upadhyay, Y.O. Halchenko, Y. Vázquez-Baeza, SciPy 1.0: fundamental algorithms for scientific computing in Python, Nat. Methods. 17 (2020) 261–272. https://doi.org/10.1038/s41592-019-0686-2.

[43] D. del-Pozo-Bueno, F. Peiró, S. Estradé, Support vector machine for EELS oxidation state determination, Ultramicroscopy. 221 (2021). https://doi.org/10.1016/j.ultramic.2020.113190.

[44] H. Kohl, A simple procedure for evaluating effective scattering cross-sections in STEM, Ultramicroscopy. 16 (1985) 265–268. https://doi.org/10.1016/0304-3991(85)90081-6.

[45] O. Grisel, A. Mueller, Lars, A. Gramfort, G. Louppe, P. Prettenhofer, M. Blondel, V. Niculae, J. Nothman, A. Joly, T.J. Fan, J. Vanderplas, manoj kumar, H. Qin, N. Hug, N. Varoquaux, L. Estève, R. Layton, J.H. Metzen, G. Lemaitre, A. Jalali, R. (Venkat) Raghav, J. Schönberger, R. Yurchak, W. Li, C. Woolam, T.D. la Tour, K. Eren, J. du Boisberranger, Eustache, scikit-learn/scikit-learn: scikit-learn 0.24.1, (2021). https://doi.org/10.5281/ZENODO.4450597.

[46] F. Pedregosa FABIANPEDREGOSA, V. Michel, O. Grisel OLIVIERGRISEL, M. Blondel, P. Prettenhofer, R. Weiss, J. Vanderplas, D. Cournapeau, F. Pedregosa, G. Varoquaux, A. Gramfort, B. Thirion, O. Grisel, V. Dubourg, A. Passos, M. Brucher, M. Perrot andÉdouardand, andÉdouard Duchesnay, Fré. Duchesnay EDOUARDDUCHESNAY, Scikit-learn: Machine Learning in Python Gaël Varoquaux Bertrand Thirion Vincent Dubourg Alexandre Passos PEDREGOSA, VAROQUAUX, GRAMFORT ET AL. Matthieu Perrot, 2011. http://scikit-learn.sourceforge.net. (accessed April 23, 2021).

[47] A.R. Symington, M. Molinari, J. Statham, J. Wu, S.C. Parker, The role of dopant segregation on the oxygen vacancy distribution and oxygen diffusion in CeO2 grain boundaries, JPhys Energy. 1 (2019). https://doi.org/10.1088/2515-7655/ab28b5.

[48] G. Arora, D.S. Aidhy, Segregation and binding energetics at grain boundaries in

fluorite oxides, J. Mater. Chem. A. 5 (2017) 4026–4035. https://doi.org/10.1039/c6ta09895a.

[49] L.A.J. Garvie, H. Xu, Y. Wang, R.L. Putnam, Synthesis of (Ca,Ce3+,Ce4+)2Ti 2O7: A pyrochlore with mixed-valence cerium, J. Phys. Chem. Solids. 66 (2005) 902–905. https://doi.org/10.1016/j.jpcs.2004.10.012.

[50] C.M. Sims, R.A. Maier, A.C. Johnston-Peck, J.M. Gorham, V.A. Hackley, B.C. Nelson, Approaches for the quantitative analysis of oxidation state in cerium oxide nanomaterials, Nanotechnology. 30 (2019). https://doi.org/10.1088/1361-6528/aae364.

[51] J. Bentley, S.R. Gilliss, C.B. Carter, J.F. Al-Sharab, F. Cosandey, I.M. Anderson, P.J. Kotula, Nanoscale EELS analysis of oxides: Composition mapping, valence determination and beam damage, J. Phys. Conf. Ser. 26 (2006) 69–72. https://doi.org/10.1088/1742-6596/26/1/016.

[52] M. Acosta, F. Baiutti, A. Tarancón, J.L. MacManus-Driscoll, Nanostructured Materials and Interfaces for Advanced Ionic Electronic Conducting Oxides, Adv. Mater. Interfaces. 6 (2019) 1–15. https://doi.org/10.1002/admi.201900462.

[53] E. Hernández, F. Baiutti, A. Morata, M. Torrell, A. Tarancón, Infiltrated mesoporous oxygen electrodes for high temperature co-electrolysis of H2O and CO2 in solid oxide electrolysis cells, J. Mater. Chem. A. 6 (2018) 9699–9707. https://doi.org/10.1039/c8ta01045e.

[54] I. Iatsunskyi, G. Gottardi, V. Micheli, R. Canteri, E. Coy, M. Bechelany, Atomic layer deposition of palladium coated TiO2/Si nanopillars: ToF-SIMS, AES and XPS characterization study, Appl. Surf. Sci. 542 (2021) 148603. https://doi.org/10.1016/j.apsusc.2020.148603.

[55] A. Kertmen, E. Barbé, M. Szkoda, K. Siuzdak, V. Babačić, P. Torruella, I. Iatsunskyi, M. Kotkowiak, K. Rytel, S. Estradé, F. Peiró, S. Jurga, Y. Li, E. Coy, Photoelectrochemically Active N-Adsorbing Ultrathin TiO 2 Layers for Water-Splitting Applications Prepared by Pyrolysis of Oleic Acid on Iron Oxide Nanoparticle Surfaces under Nitrogen Environment, Adv. Mater. Interfaces. 6 (2019) 1–10. https://doi.org/10.1002/admi.201801286.

[56] H.H. El-Maghrabi, A.A. Nada, M.F. Bekheet, S. Roualdes, W. Riedel, I. Iatsunskyi, E. Coy, A. Gurlo, M. Bechelany, Coaxial nanofibers of nickel/gadolinium oxide/nickel oxide as highly effective electrocatalysts for hydrogen evolution reaction, J. Colloid Interface Sci. 587 (2021) 457–466. https://doi.org/10.1016/j.jcis.2020.11.103.

[57] Z. Hou, W. Pei, X. Zhang, K. Zhang, Y. Liu, J. Deng, L. Jing, H. Dai, Rare earth oxides and their supported noble metals in application of environmental catalysis, J. Rare Earths. 38 (2020) 819–839. https://doi.org/10.1016/j.jre.2020.01.011.

[58] J.J. Sánchez, M. López-Haro, J.C. Hernández-Garrido, G. Blanco, M.A. Cauqui, J.M. Rodríguez-Izquierdo, J.A. Pérez-Omil, J.J. Calvino, M.P. Yeste, An atomically efficient, highly stable and redox active Ce0.5Tb0.5O: X (3% mol.)/MgO catalyst for total oxidation of methane, J. Mater. Chem. A. 7 (2019) 8993–9003. https://doi.org/10.1039/c8ta11672e.

[59] D.M. Tobaldi, L. Lajaunie, M. López Haro, R.A.S. Ferreira, M. Leoni, M.P. Seabra, J.J. Calvino, L.D. Carlos, J.A. Labrincha, Synergy of Neodymium and Copper for Fast and Reversible Visible-light Promoted Photochromism, and Photocatalysis, in Cu/Nd-TiO2 Nanoparticles, ACS Appl. Energy Mater. 2 (2019)

3237–3252. https://doi.org/10.1021/acsaem.9b00084.

[60] M.A. Roldan, A. Mayence, A. López-Ortega, R. Ishikawa, J. Salafranca, M. Estrader, G. Salazar-Alvarez, M. Dolors Baró, J. Nogués, S.J. Pennycook, M. Varela, Probing the meta-stability of oxide core/shell nanoparticle systems at atomic resolution, Chem. Eng. J. 405 (2021) 126820. https://doi.org/10.1016/j.cej.2020.126820.

[61] P. Torruella, A. Ruiz-Caridad, M. Walls, A.G. Roca, A. López-Ortega, J. Blanco-Portals, L. López-Conesa, J. Nogués, F. Peiró, S. Estradé, Atomic-Scale Determination of Cation Inversion in Spinel-Based Oxide Nanoparticles, Nano Lett. 18 (2018) 5854–5861. https://doi.org/10.1021/acs.nanolett.8b02524.